PERGAMON

Journal of Structural Geology 24 (2002) 999–1011

JOURNAL OF STRUCTURAL GEOLOGY

www.elsevier.com/locate/jstrugeo

Some garnet microstructures: an illustration of the potential of orientation maps and misorientation analysis in microstructural studies

David J. Prior[a,*], John Wheeler[a], Luca Peruzzo[b], Richard Spiess[b], Craig Storey[c]

[a]*Department of Earth Sciences, Liverpool University, Liverpool L69 3BX, UK*
[b]*Dipartimento di Mineralogia e Petrologia, Corso Garibaldi 37, 35137 Padova, Italy*
[c]*Department of Geology, University of Leicester, Leicester LE1 7RH, UK*

Received 2 February 2001; revised 18 June 2001; accepted 24 June 2001

Abstract

The microstructures of two contrasting garnet grains are mapped using automated electron backscatter diffraction. In both cases there is a very strong crystallographic preferred orientation, with measurements clustered round a single dominant orientation. Each garnet grain is divided into domains with similar orientations, limited by boundaries with misorientations of 2° or more. In both samples most of misorientation angles measured across orientation domain boundaries are significantly lower than those measured between random pairs of orientation domains. One sample is a deformed garnet that shows considerable distortion within the domains. Lines of orientation measurements within domains and across domain boundaries show small circle dispersions around rational crystallographic axes. The domain boundaries are likely to be subgrain boundaries formed by dislocation creep and recovery. The second sample is a porphyroblast in which the domains have no internal distortion and the orientation domain boundaries have random misorientation axes. These boundaries probably formed by coalescence of originally separate garnets. We suggest that misorientations across these boundaries were reduced by physical relative rotations driven by boundary energy. The data illustrate the potential of orientation maps and misorientation analysis in microstructural studies of any crystalline material.

Keywords: Garnet; Microstructure; Electron backscatter diffraction (EBSD); Orientation map; Misorientation

1. Introduction

In the 150 years of microstructural studies, significant advances have often been facilitated by technological developments. The petrological microscope, the electron probe microanalyser and the transmission electron microscope are now established tools that we rely upon. The development of electron backscatter diffraction (EBSD) (Venables and Harland, 1973; Dingley, 1984, 2000) in the scanning electron microscope (SEM) is allowing new lines of investigation of material microstructures. EBSD enables crystallographic orientations of micrometre-sized points to be measured easily, precisely and quickly (Prior et al., 1999; Schwartz et al., 2000). Other methods can be used to measure bulk rock crystallographic preferred orientations (CPOs) (Leiss et al., 2000; Randle and Engler, 2000), but the real power of the EBSD approach comes from its ability to explore the spatial variation of lattice orientations in any crystal system. This is achieved using gridded EBSD data (Adams et al., 1993) to produce orientation maps or by locating individual EBSD analyses using qualitative orientation contrast (OC) images (Prior et al., 1996; Bartozzi et al., 2000). Moreover, we can determine the crystallographic misorientation between any two orientation measurements (Lloyd et al., 1997; Randle and Engler, 2000; Wheeler et al., 2001) and EBSD is the first technique with the potential to collect statistically significant misorientation data sets with ease. The aim of this short paper is to illustrate the potential of these techniques in microstructural studies.

Garnet is optically isotropic and statistically significant garnet substructures had not been documented before the advent of forescatter OC imaging and EBSD. It is now clear that they are relatively common (Prior et al., 1996, 1999, 2000; Spiess et al., 2001). To show how the spatial variation of lattice orientations and the misorientation characteristics of a sample can help constrain processes, and to discuss current technological limitations, we present garnet microstructure data from two contrasting samples.

2. Methods

SYTON-polished (Fynn and Powell, 1979; Lloyd, 1987;

* Corresponding author.
E-mail address: davep@liverpool.ac.uk (D.J. Prior).

0191-8141/02/$ - see front matter
PII: S0191-8141(01)00087-6

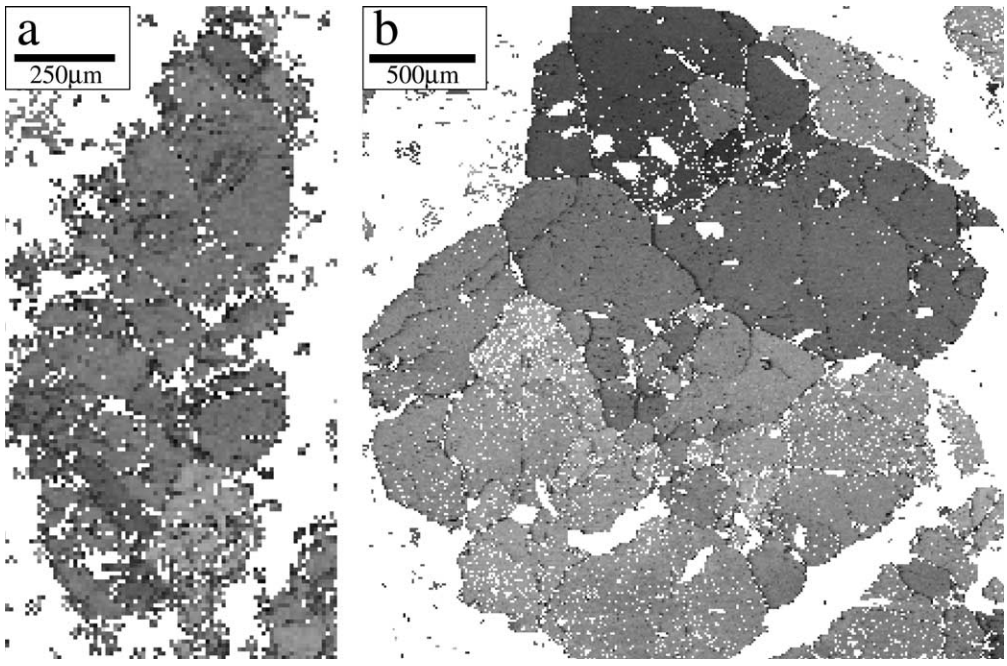

Fig. 1. Pattern quality maps. These pixels of the maps have intensity that corresponds to the band contrast in the EBSD pattern. Band contrast is an image analysis parameter that corresponds to pattern quality. Dark pixels have poor pattern quality, bright pixels good pattern quality. Pixels that gave no indexing solution are white. Lone pixels (see text) have been removed. Areas outwith of the central area of garnet, of each map, were excluded manually from analysis. These areas comprise neighbouring garnet grains (bottom right of (a) and bottom right and top right of (b)) and scattered areas of other minerals incorrectly indexed as garnets. Areas excluded from analysis can be evaluated by comparison with Fig. 2. (a) Glenelg garnet. (b) Alpine garnet.

Prior et al., 1996) thin sections were analysed in a CamScan X500 crystal probe fitted with a thermionic field emission gun and a FASTRACK stage. We used an accelerating voltage of 20 kV, a beam current of 5 nA and a working distance of about 26 mm. The samples we analysed were uncoated. Although orientation mapping is possible in garnet without a conductive coat, other minerals, such as calcite, need to have a thin carbon coat for good results. EBSD patterns were collected on rectangular grids with 10 μm spacing between data points. OC images showed that the samples contained sub-domains of down to about 20 μm in size, with most sub-domains being larger than this. A 10 μm grid spacing was chosen so that more than one measurement was made in each sub-domain. A finer grid spacing would have given better detail in small sub-domains, but would have required much longer acquisition times. Patterns were acquired and automatically indexed using the program Channel 4.2 from HKL software. Between four and six bands in the diffraction pattern were picked, automatically, using the Hough transform routine in the Channel 4.2 program. The program then searched for an indexing solution: a lattice orientation, for the mineral structure input into the program, that would generate the diffraction bands picked, within a small angular tolerance ($<3°$). After an indexing solution was found, or the software abandoned attempts to find a solution, the stage was moved 10 μm and a new pattern collected. EBSD maps can also be made by moving the beam rather than the stage. Beam scanning is faster than stage scanning but has the disadvantage that the EBSD calibration (see Prior et al., 1999), the activation volume geometry and the beam focus change as the beam incidence point moves. As a consequence, beam scan maps are lower in quality than stage scan maps and are limited to relatively small areas (this depends upon hardware but is generally a few hundred micrometres field of view). Unlike metals, where beam scans can work at up to about 25 points per second (P. Trimby pers. comm.), most rock-forming minerals require something of the order of 0.5 s or more in pattern acquisition and indexing. The FASTRACK stage we used can move fast enough to analyse about four points per second so that stage scan of garnet is not significantly slower than beam scan. In this study, only the garnet structure was input into the indexing software and EBSD patterns from other phases could not be solved correctly. Data were collected at a rate of about 0.8 s per measurement point. Maps (Figs. 1–3) were constructed by assigning a colour or grey shade to a pixel representing each measurement point. The grey shade or colour relates to a quantitative image analysis parameter of the EBSD pattern (Fig. 1) or to some aspect of orientation calculated from the EBSD pattern, such as the misorientation angle between each data point and a fixed reference point (Fig. 2a and c). Maps of orientation data can be processed. One aim of processing is to remove erroneous data. A second aim is to provide a more complete microstructural reconstruction of the sample (Fig. 3). Application of processing algorithms does create a risk of introducing artefacts into the data — this point will be discussed later. In

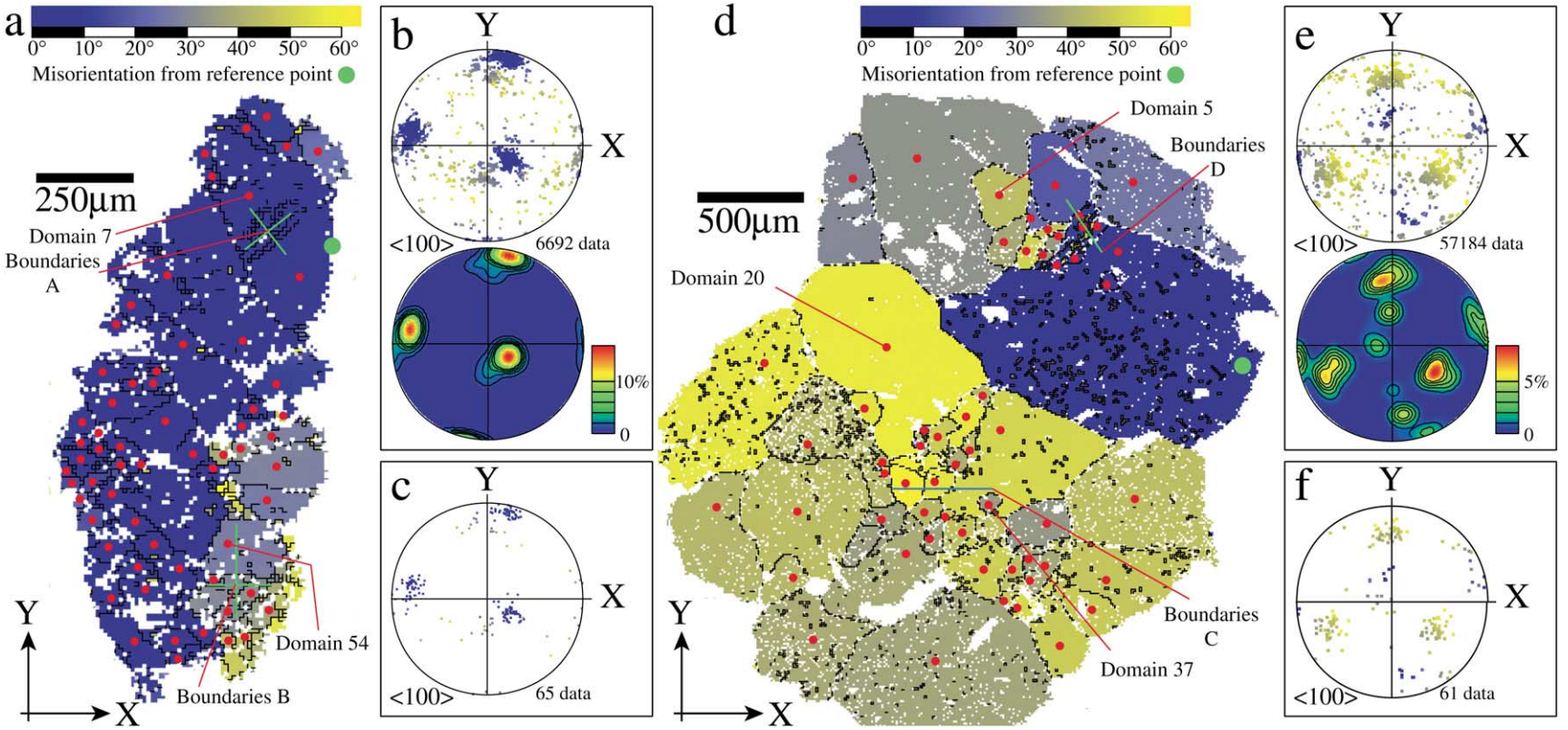

Fig. 2. Orientation maps and corresponding pole figures for two garnets. (a)–(c) Data from a garnet in a shear zone from Glenelg. (d)–(f) Data from a Type 2 garnet porphyroblast (see Spiess et al. (2001) for terminology) from the Alps. In the orientation maps (a, d) each pixel represents an orientation measured from an EBSD analysis. Data are on a grid with a 10 μm spacing. White areas are points that were not indexed, or have been removed manually (areas shaded in Fig. 1 and white here). These are mostly phases other than garnet. Lone pixels have been removed automatically (see text). The pixels of garnet are coloured according to their angular misorientation from the point marked with a green dot. Black lines are drawn between any two adjacent points with a misorientation >2°. Continuity of these shows significant boundaries with >2° misorientation that correspond with poor pattern quality along grain boundaries (Fig. 1). Red dots are placed on the measurements selected to represent orientation domains for misorientation analysis. Labelled green lines and domains correspond to data subsets shown in Figs. 6 and 7. The map orientation reference frame *XYZ* (*Z* out of page) is shown next to the maps and is marked on the pole figures (b, c and e, f). Pole figures are equal area lower hemisphere stereonets showing the ⟨100⟩ orientations. The pole figures in (b) and (e) show all the measurements represented as pixels in the maps shown in (a) and (d), respectively. Points in the upper net (three points for each measurement) have colours that correspond to the map. The lower net is contoured and the scale shows intensity as multiples of uniform distribution. The pole figures in (c) and (f) are equal area lower hemisphere stereonets showing the ⟨100⟩ orientations of the orientation domains selected from the maps shown in (a) and (d), respectively. Points have colours that correspond to the map.

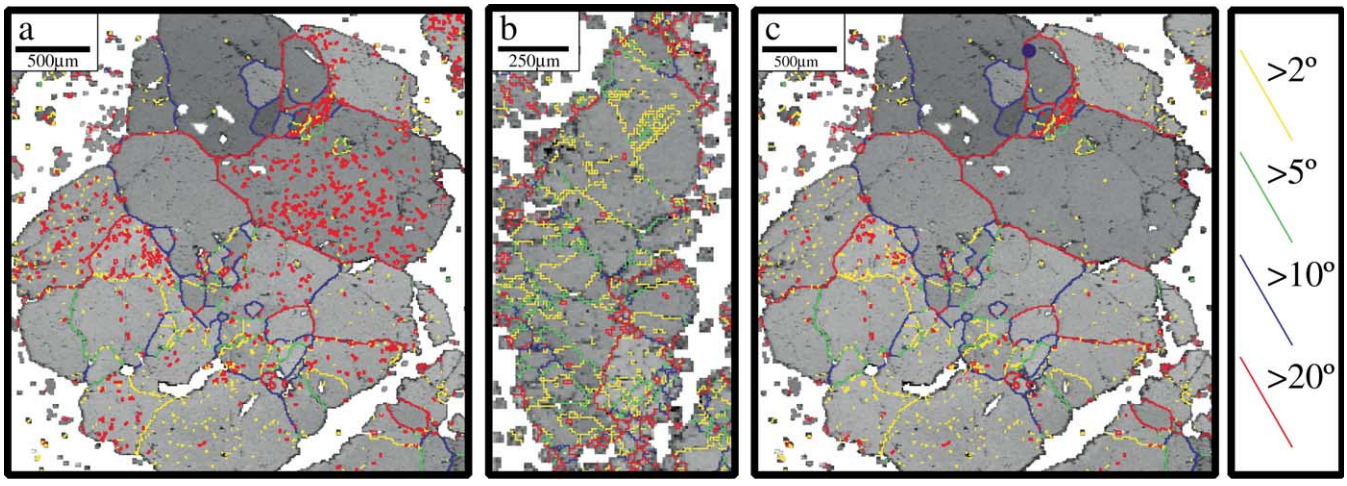

Fig. 3. Processed maps to highlight misorientation boundaries. The maps are pattern quality maps (as Fig. 1) with coloured lines to show misorientations between neighbouring pixels superposed. Key to misorientation angles is on the right. All images have had lone pixels removed and non-indexed pixels have been allowed to take the dominant orientation of neighbouring pixels. Comparison with Fig. 1 shows that there are larger areas of pixels around the margins of the central garnets in the processed images in this figure. These areas have grown as a result of the processing and are artefacts. Further processing has been carried out to generate the maps in (b) and (c) to reduce systematic mis-indexing problems. Pixels misoriented from most of their neighbours by certain special misorientation angles and axes have been rotated to the same orientation as most of their neighbours. The axes and angles used were: 27 ± 3° around ⟨100⟩ ± 5°, 27 ± 3° around ⟨112⟩ ± 5°, 27 ± 3° around ⟨124⟩ ± 5° and 60 ± 3° around ⟨111⟩ ± 5°. (a) Alpine garnet. Isolated red spots (also seen as black spots in Fig. 2) in many areas relate to mis-indexed pixels. Many of these are systematically mis-indexed. The degree of mis-indexing depends upon orientation. Some orientation domains have little mis-indexing, some a lot. (b) Glenelg garnet. (c) Alpine garnet. Comparison with (a) shows the effectiveness of processing to remove systematically mis-indexed data.

preparation of the maps and data in Fig. 2, automated processing was limited to the removal of data points that were misoriented from all eight neighbouring measurements by more than 5°. As long as the grid size is picked so that several pixels occupy each orientation domain, then lone data points are likely to be erroneous and removal of these should improve the data without introducing artefacts.

Comparison of orientation maps to BSE and transmitted light images were used to assess the number of other minerals incorrectly indexed as garnet. 13–18% of measurements in minerals other than garnet were incorrectly indexed as garnet. This figure was reduced to 1–5% (average 2%) by removing all lone data points. Remaining points that were wrongly indexed as garnet were filtered out manually, by comparison with a BSE image. 85–100% (depending upon orientation: average 90%) of measurements in garnet gave indexing solutions. Comparison of automated data with data collected manually, using OC images to show the garnet sub-domains (see Spiess et al., 2001) enabled the levels of mis-indexing to be assessed. Between 0 and 12% (depending upon garnet orientation) of solutions in garnet were indexed incorrectly. The maximum percent of mis-indexing was reduced to 7% by removing all lone data points. After this processing, we estimate that 2–3% of the indexing solutions within all garnet measurements were wrong.

Misorientations of >2°, calculated between neighbouring measurements are shown as black lines on the maps (Fig. 2a and d). Orientation domains, for use in misorientation analysis, were defined from the maps. Here, an orientation domain is an area enclosed within boundaries with >2° misorientation. This angle was chosen as this is the minimum misorientation that can be reliably identified using the EBSD method (Prior, 1999; Humphreys et al., 2001). Changes of misorientation along boundaries and boundary topology make the choice of orientation domains rather subjective (Fig. 2). However, pole figures constructed using one measurement to represent each orientation domain (Fig. 2c and f) show the same pattern as pole figures from all indexed solutions in each garnet (Fig. 2b and e). Neighbour pair misorientations (Wheeler et al., 2001) were calculated between orientation domains with a common boundary. Random pair misorientations (op. cit.) were calculated from random pairs of orientation domains. The random pairs could include some neighbouring orientation domains but will be dominated by non-neighbouring pairs. Histograms show neighbour and random pair misorientation angle distributions (Fig. 4a and c) and inverse pole figures show neighbour pair misorientation axes (Fig. 4b and d).

Ideally we want to avoid the manual, and therefore subjective, selection of orientation domains in the generation of misorientation data. However, this is problematic. Pattern quality (Fig. 1) tends to be low at grain boundaries. As a result, indexing solutions are often missing along grain boundaries and in an analysis of misorientations of adjacent pixels, real boundaries will be under-represented. Further processing of the maps is needed. A simple algorithm, available through the Channel 4.2 software, allows non-indexed pixels to take on the orientation of the most common neighbour orientation. As long as non-indexed

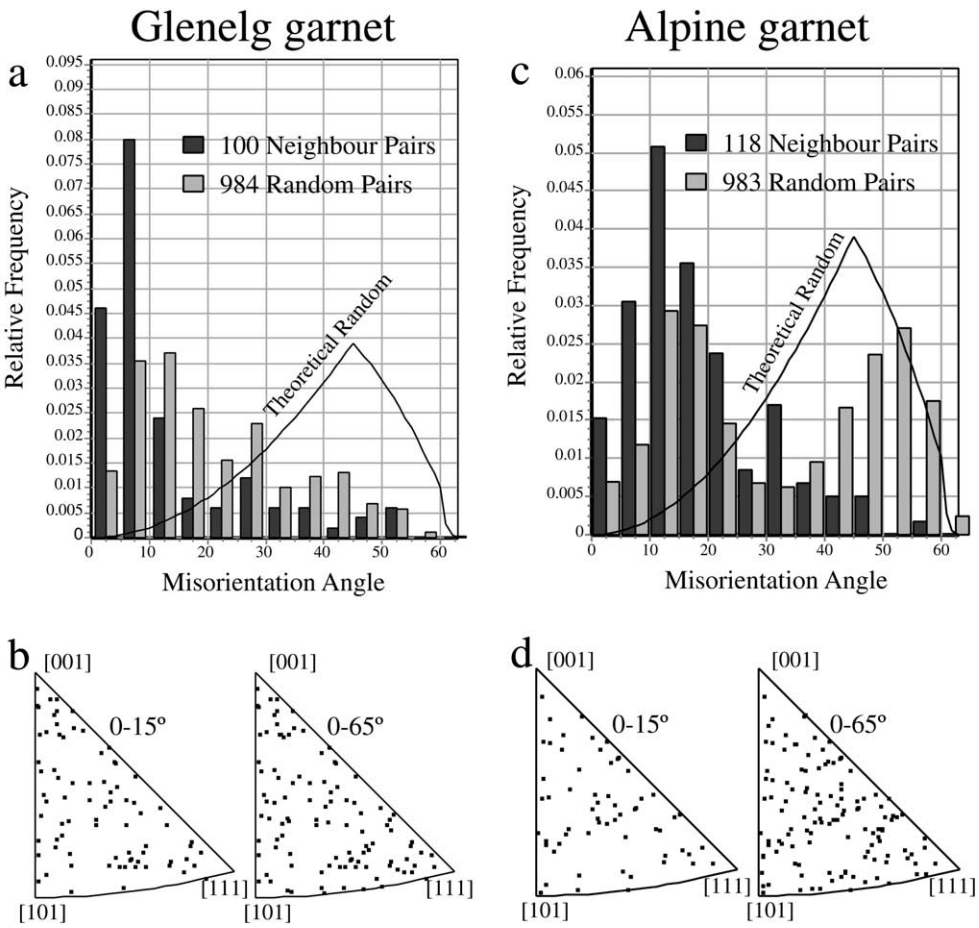

Fig. 4. Misorientation data for the Glenelg garnet (a, b) and the Alpine Garnet (c, d). Misorientation angle distributions in (a) and (c) are calculated from the orientation domain data shown in Fig. 2c and f, respectively. Dark columns are the misorientations across boundaries between neighbouring orientation domains. Pale columns are the misorientations between randomly picked pairs of orientation domains. The black line is the expected distribution for a random orientation distribution (see Wheeler et al., 2001). Misorientation axes (b, d) are plotted in inverse pole figures (upper hemisphere, equal angle) for misorientations measured across boundaries between neighbouring orientation domains. One plot shows only misorientations with magnitudes up to 15°, the other shows all the data.

areas are not significantly larger than 1 pixel and the indexing rate is high (>80%) the artefacts generated by this processing should be minimised and errors on the position of any boundary will be up to ~2× the step size. Although such processing produces much cleaner misorientation boundary maps (Fig. 3), artefacts are generated around the margins of the mapped garnets and these artefacts need to be excluded manually from any analysis (e.g. the data in Fig. 5: see caption). Plotting the misorientation data of neighbouring pixels in processed data from the Alpine garnet (Fig. 5) highlights another problem. Although the proportion of pixels incorrectly indexed is so small that it does not affect the CPO (compare Fig. 2e and f, for example), many of the pixels have been mis-indexed systematically and impact significantly on the misorientation data (Fig. 5). The misorientation angle distribution (Fig. 5a) has peaks at about 27 and 60° that correspond to systematic mis-indexing problems. The 27° peak corresponds to ⟨001⟩, ⟨112⟩ and ⟨142⟩ apparent misorientation axes (Fig. 5b), whereas the 60° peak corresponds to ⟨111⟩ apparent misorientation axes (Fig. 5c). The data points that give rise to the mis-indexing problems are easy to see in the Alpine garnet. They appear as isolated pixels surrounded by boundaries (Figs. 2d and 3a). They are not so clear in the Glenelg garnet (Fig. 2a). It is possible to correct for mis-indexing, by removing boundaries of known geometry, as long as there are no significant real boundaries that have that geometry. The maps in Fig. 3 show misorientations of >2, >5, >10, >15 and >20° calculated between neighbouring pixels after processing (using Channel 4.2) to fill non-indexed areas in the boundaries. The maps in Fig. 3b and c have been processed further, to remove systematic mis-indexing problems (see caption for details). Misorientation data from these processed maps (Fig. 5d) are very similar to those calculated from manually picked orientation domains (Fig. 3d). Although this gives us confidence that the processing applied here has not introduced significant artefacts and that we could use these misorientation data, the

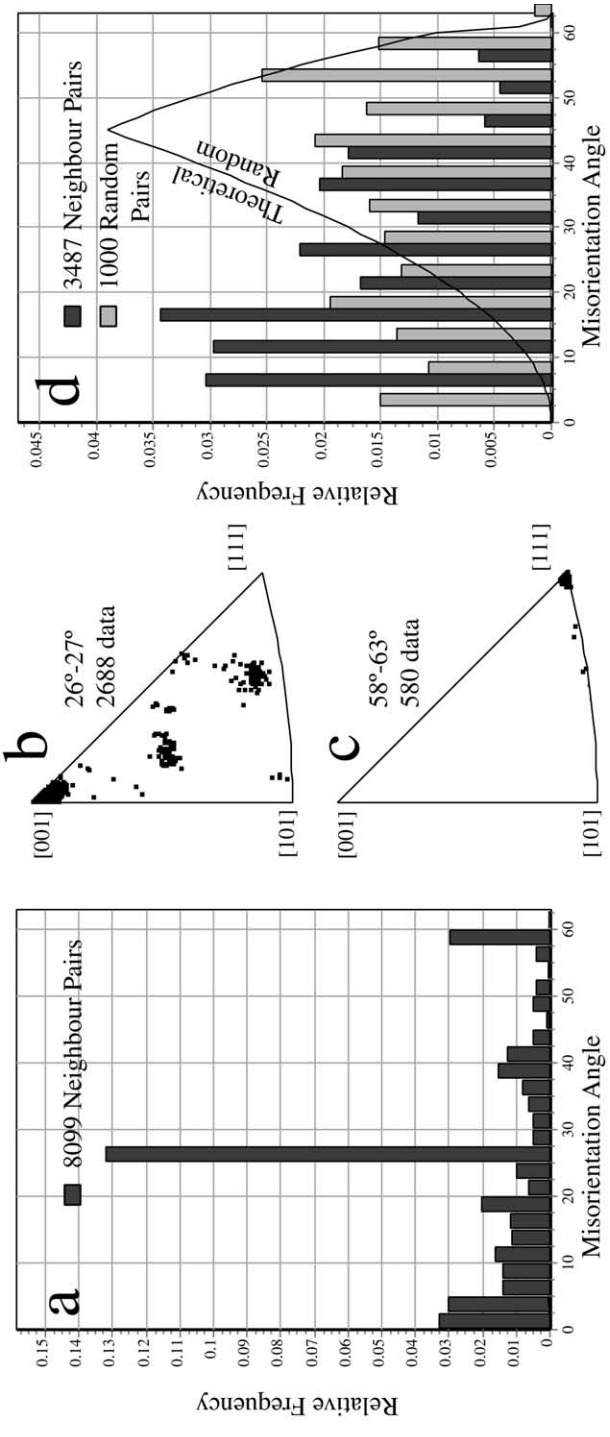

Fig. 5. Misorientation data for the Alpine garnet taken directly from the maps, without manual definition of orientation domains. (a) Neighbour pair misorientation angle distributions (>2°) calculated from all neighbouring pixels, after processing to fill in grain boundaries, but with no processing to remove systematically mis-indexed pixels. The data correspond to the coloured area shown in Fig. 2d but processed to the level shown in Fig. 3a. (b) Neighbour pair misorientation axes corresponding to 26–27° misorientation angles shown in (a). (c) Neighbour pair misorientation axes corresponding to 58–63° misorientation angles shown in (a). (d) Neighbour and random pair misorientation angle distributions (>2°) calculated from all neighbouring pixels, after processing to remove systematically mis-indexed pixels as outlined in the caption to Fig. 3. The data correspond to the coloured area shown in Fig. 2d but processed to the level shown in Fig. 3c.

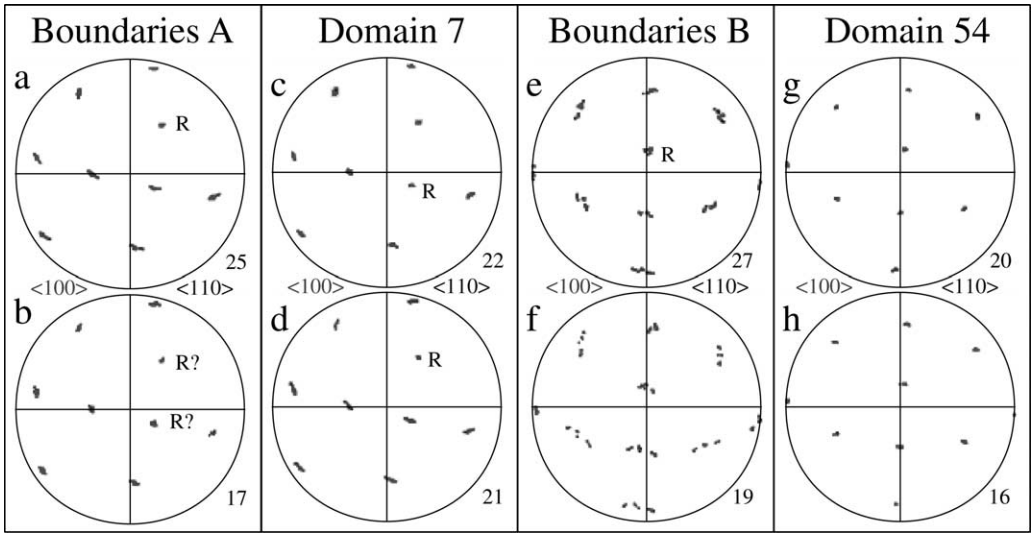

Fig. 6. Equal area lower hemisphere stereonets showing the ⟨100⟩ (pale grey: three points per measurement) and ⟨110⟩ (dark grey: six points per measurement) orientations for data collected in lines one pixel wide from the orientation map of the Glenelg garnet (Fig. 2a). Where the data show dispersion around a rotation axis, the axis is marked R. Numbers at the bottom indicate number of measurements. (a, b) Data from a NW oriented line (a) and a SE oriented line (b), shown in green, near the top of the orientation map in Fig. 2a. The NW line crosses a series of low angle boundaries between two orientation domains. (c, d) Data from a vertical line (c) and a horizontal line (d) within orientation domain 7 (labelled in Fig. 2a). (e, f) Data from vertical (e) and horizontal (f) lines, shown in green, near the bottom of the orientation map in Fig. 1a. Both lines cross several low angle boundaries and orientation domains. (g, h) Data from a vertical line (g) and a horizontal line (h) within orientation domain 7 (labelled in Fig. 2a).

misorientation data used to interpret garnet microstructures will be that based on the manual selection of orientation domains (Fig. 4).

3. Garnet microstructures

Two samples with contrasting garnet microstructures are examined in this paper. The first is a typical deformed garnet porphyroclast in an upper-amphibolite facies shear zone that affects the eclogites of the Glenelg–Attadale inlier of NW Scotland (Storey et al., work in progress). The second sample a typical garnet porphyroblast from the Schneeberg Complex of the N. Italian Alps (Peruzzo, 1998; Spiess et al., 2001).

3.1. Orientation maps

The orientation maps (Fig. 2a and d) show qualitative differences between the two samples. The Glenelg garnet has a domainal microstructure in which orientation domains are relatively poorly defined (Fig. 2a). Each orientation domain is internally distorted. In contrast, the Alpine garnet porphyroblast contains relatively regular orientation domains with minimal internal distortion (Fig. 2d). Orientation data alone would not illustrate this: the orientation distributions of the two samples are similar. Both comprise clustering close to a single orientation (Fig. 2b, c, e and f).

3.2. Misorientation angle distribution

The random pair misorientation angle distribution does not correspond to that predicted for a random orientation distribution in either sample. This is because both have strong CPOs. In the Glenelg garnet the random pair misorientations are smoothy distributed with a maximum at about 15° (Fig. 4a). In the Alpine garnet the random pair misorientation distribution is bimodal with peaks at about 15 and 55° (Fig. 4c). In both samples the neighbour pair misorientation angle distribution is biased towards low misorientations (Fig. 4a and c) and is different to the random pair misorientation angle distribution. The bulk of boundaries in the Glenelg garnet have misorientations less than 10° (Fig. 4a), whereas the bulk of boundaries in the Alpine garnet have misorientations less than 20° (Fig. 4c). This difference in the boundary misorientations can also be seen in the processed boundary maps (Fig. 3b and c). The Glenelg garnet (Fig. 3b) is dominated by 2–5° and 5–10° boundaries. The Alpine garnet (Fig. 3c) has more 10–20° and >20° boundaries.

3.3. Misorientation axis distribution

The misorientation axis distributions of the two samples appear similar. Both are apparently random (Fig. 4b and d). A more careful look at the spatial distribution of orientations shows that the true nature of the misorientation axis distributions may be masked by errors. The orientations in the Glenelg garnet vary from each pixel to a neighbouring pixel. During data acquisition the EBSD pattern shifts slightly each time the sample point changes. Although the misorientation axes appear random, the orientations of all the pixels in a line up to 300 μm (30 pixels) long often show

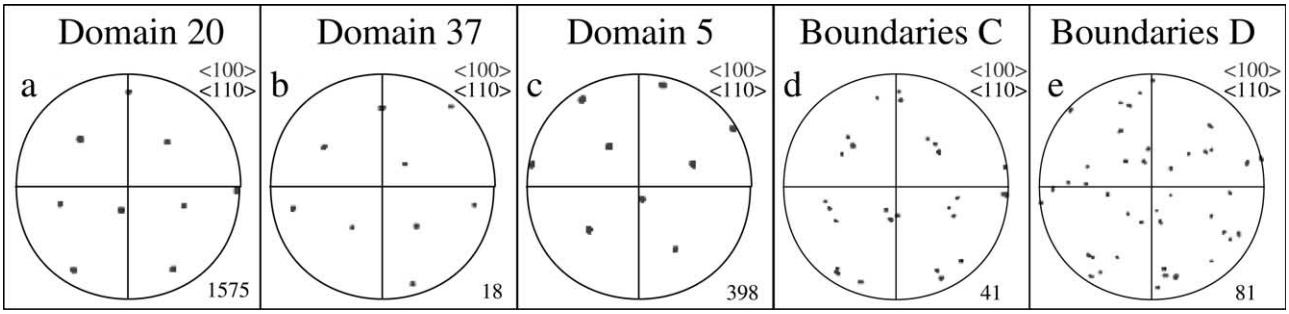

Fig. 7. (f)–(j) Equal area lower hemisphere stereonets showing the ⟨100⟩ (pale grey: three points per measurement) and ⟨110⟩ (dark grey: six points per measurement) orientations for data collected from areas (a)–(c) or lines one pixel wide (d, e) from the orientation map of the Alpine garnet (Fig. 2d). Numbers at the bottom indicate number of measurements. (a) Data from an area in a large orientation domain (20: marked in Fig. 2d). (b) Data from an area in a small orientation domain (37: marked in Fig. 2d). (c) Data from an area in a medium orientation domain (5: marked in Fig. 2d). (d) Data from a horizontal line, shown in green in the lower half of Fig. 2d, which crosses two domain boundaries and includes three domains. (e) Data from a NW line, shown in green in the lower half of Fig. 2d, which crosses four domain boundaries and includes five domains.

continuous small-circle dispersions with a rational crystallographic axis as the apparent misorientation axis (Fig. 6). This can be true for lines that cross low angle (>2°) boundaries (Fig. 6a, b and e) and for lines entirely within orientation domains (Fig. 6c and d). The degree of dispersion is different in different locations. For example, the dispersion in domain 54 (Fig. 6g and h) is much less than the dispersion in domain 7 (Fig. 6a and b). Lines of different orientation at the same location can give different degrees of dispersion and different apparent misorientation axes. For example, orientations measured on a horizontal line in domain 7 (Fig. 6d) show clear dispersion around a ⟨110⟩ axis. The data from a vertical line in the same domain show less clear dispersion around a ⟨100⟩ axis (Fig. 6c). The effect of line orientation can also be seen comparing the data shown in Fig. 6a with those in Fig. 6b and comparing the data in Fig. 6e with those in Fig. 6f. A consequence of the difference in dispersion with the line orientation is that the orientations corresponding to areas, rather than lines, of pixels give rise to dispersions with no clear misorientation axis. The neighbour pair misorientation axes (Fig. 4b) do not show the clear crystallographic control apparent from dispersion of orientation data. The reason for this is that the errors on a misorientation axis, calculated from two orientations with a small misorientation angle, are large (Prior, 1999). If the errors on misorientation axes can be substantially reduced (Prior, 1999), it is likely that the inverse pole figure of misorientation axes will show a strong, non-random distribution. Statistical averaging of misorientation axes for linear transects of data (Wheeler et al., work in progress) should enable better constraints on the misorientation axis distribution.

A similar analysis of the Alpine garnet highlights the contrasts between the two samples. In this case, during acquisition, the EBSD pattern does not move as the measurement point changes within a single orientation domain. The scatter of measured orientations within an orientation domain represents analytical error on the orientation (~0.5–1°). All of the measurements within any single orientation domain give one single orientation with very little dispersion (Fig. 7a–c). This is true for small (Fig. 7b), medium (Fig. 7c) and large (Fig. 7a) orientation domains. Measurements along lines that cross boundaries (>2°) give rise to discrete sets of points on a pole figure (Fig. 7d and e: each set corresponds to the orientation of one domain) rather than to a continuous dispersion. The misorientations across boundaries, although statistically biased towards small misorientations, contain a significant proportion of boundaries with >10° misorientation (Figs. 3c and 4c). These have mean misorientation axis errors of less than ~4° and maximum misorientation axis errors of less than ~12° (Prior, 1999). In this case, the misorientation axis distribution is likely to be truly random. In this sample, reducing the errors on the misorientations across low angle boundaries will be possible by averaging the orientations of all the measurements within each orientation domain and then calculating misorientations between these average orientations (Humphreys et al., 2001).

4. Interpretation of the processes responsible for the observed microstructures

The fact that we can document substructures within these garnets means that their histories must be more complex (or at least different) than that which we would infer from conventional (optical and microprobe) data alone. TEM data can be used to image garnet substructures (Voegelé et al., 1998b), although it is difficult to assess their scale and statistical significance. The best interpretation of the processes responsible for the observed garnet microstructures requires more than just the EBSD data. The interpretations of process presented here have been made using the EBSD data in conjunction with light optical and EPMA compositional data (Spiess et al., 2001; Storey et al., work in progress) that we do not present here for reasons of brevity. The preferred models explain the misorientation characteristics of the observed microstructures.

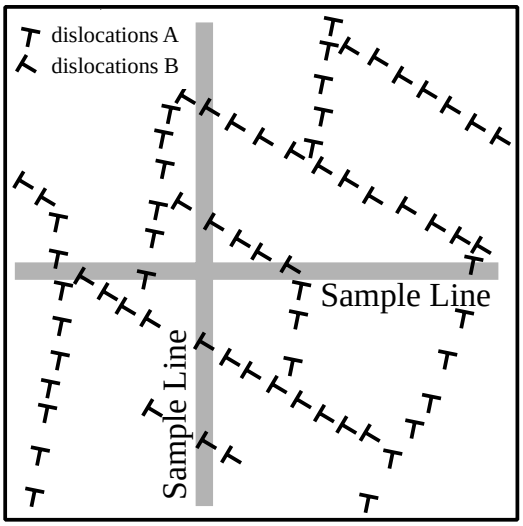

Fig. 8. Illustration of the effect subgrain boundary structures will have on dispersions of orientation data. Dislocations A and B are different. A falls dominantly into boundaries of one orientation and B into boundaries of a different orientation. In this case the vertical sample line crosses mainly boundaries of dislocation B and the orientations will show dispersion related to the geometry of dislocation B. The horizontal sample line crosses mainly boundaries of dislocation A and the orientations will show dispersion related to the geometry of dislocation A. Data from the whole boxed area will have more complex dispersions related to the combined geometries of A and B.

4.1. Glenelg garnet

Continuous small-circle dispersions of orientations are explained by plastic strain of the lattice, along the line of measurements, controlled by dislocations (Lloyd and Freeman, 1991, 1994; Boyle et al., 1998; Leiss and Barber, 1999; Prior et al., 1999). The dislocations may be distributed or arranged in subgrain boundaries and the fact that small-circle dispersions are observed for transects that cross low angle boundaries suggests that this is true. The difference in dispersions for different line orientations at the same locality also supports this interpretation. Dislocations of a particular geometry tend to fall into boundaries of a particular orientation. As a consequence, linear tracks of measurements tend to cross boundaries dominated by dislocations of one particular geometry (Fig. 8) and measurements from an area, which will contain a mix of dislocation geometries, will give dispersions without clear misorientation axes. The best interpretation of the Glenelg garnet microstructure is that it is a single garnet that has deformed by dislocation creep, accompanied by recovery. The average orientation probably reflects the orientation of the garnet before deformation (although this may have been modified by rigid rotations). Low angle boundaries are likely to be subgrain boundaries whose geometry is a function of the original garnet orientation and the dislocation slip systems.

Misorientation axes (in this case the rotation axes defined by dispersions) can be used to constrain important slip systems (Lloyd and Freeman, 1991, 1994; Lloyd et al., 1997; Boyle et al., 1998; Leiss and Barber, 1999; Prior et al., 1999). Because the orientation maps also constrain the orientations of low angle boundaries, a more sophisticated analysis of slip systems can be made here. Fig. 9a enlarges part of Fig. 2a to show low angle boundaries that give rise to clear dispersions around one $\langle 110 \rangle$ direction (Fig. 6a). If the boundaries are tilt walls (Fig. 9b), the boundary planes must contain the mapped boundary trace (Fig. 9a and c) and the misorientation axis (Fig. 9c). Alternatively, if they are twist walls, the misorientation axis must be normal to the boundary plane. The normal to the misorientation axis does not give the observed boundary trace (Fig. 9d), whereas we can draw a subgrain boundary plane that contains the boundary trace and the misorientation axis (Fig. 9e). Thus, a tilt wall model is consistent with the observational data whilst a twist wall model is not. Two reconstructed boundary orientations (Fig. 9d) are constructed from the two most extreme boundary trace orientations (Fig. 9a). If the dislocations comprise a population of one type of edge dislocation, then the misorientation axis should lie in the slip plane perpendicular to the slip vector (Fig. 9b). Known garnet slip systems (Voegelé et al., 1998a,b) are $\frac{1}{2}\langle 111 \rangle \{1\,-\,10\}$, $\frac{1}{2}\langle 111 \rangle \{1\,-\,12\}$, $\frac{1}{2}\langle 111 \rangle \{12\,-\,3\}$, $\langle 100 \rangle \{010\}$, and $\langle 100 \rangle \{011\}$. A $\{12\,-\,3\}$ plane does not contain a $\langle 110 \rangle$ direction so that a simple geometry of $\frac{1}{2}\langle 111 \rangle \{12\,-\,3\}$ dislocations cannot give rise to $\langle 110 \rangle$ misorientation axes. Sets of identical $\frac{1}{2}\langle 111 \rangle \{1\,-\,12\}$ or $\langle 100 \rangle \{011\}$ edge dislocations would give $\langle 110 \rangle$ misorientation axes. If we suppose that both $\langle 111 \rangle$ slip directions in a $\{1\,-\,10\}$ plane were present in equal numbers in a subgrain boundary, so that the resultant slip vector were $\langle 001 \rangle$, then a $\langle 110 \rangle$ misorientation axis could result. Similarly, if dislocations with both $\langle 100 \rangle$ slip directions in a $\{010\}$ plane were present in equal numbers in a subgrain boundary then a $\langle 110 \rangle$ misorientation axis could result. Although these last two scenarios seem unlikely we will include them in further analysis. Subgrain boundaries in cubic crystals are likely to have orientations at high angles to the slip plane (Fig. 6b). We can use this geometry to assess the compatibility of viable slip systems with the observations. To make discussion easier we assign specific indices to the crystal orientation (Fig. 9f), so that the misorientation axis is [110] and the $\langle 100 \rangle$ nearest specimen Y is [100]. The (-110) plane passes through the misorientation axis and subtends angles of 45 and 55° to the two reconstructed subgrain boundary planes (Fig. 9g) suggesting that the boundaries are unlikely to comprise either $[100](-110)$ dislocations or $\frac{1}{2}([111](-110) + [-1\,-\,11](-110))$ edge dislocations. The (001) plane passes through the misorientation axis and has angles of 35 and 45° to the two reconstructed subgrain boundary planes (Fig. 9h), suggesting that the boundaries are unlikely to comprise $([010](001) + [-100](001))$ edge dislocations. The (-112) and $(-11\,-\,2)$ planes pass through the misorientation axis. The $(-11\,-\,2)$ plane is coincident with

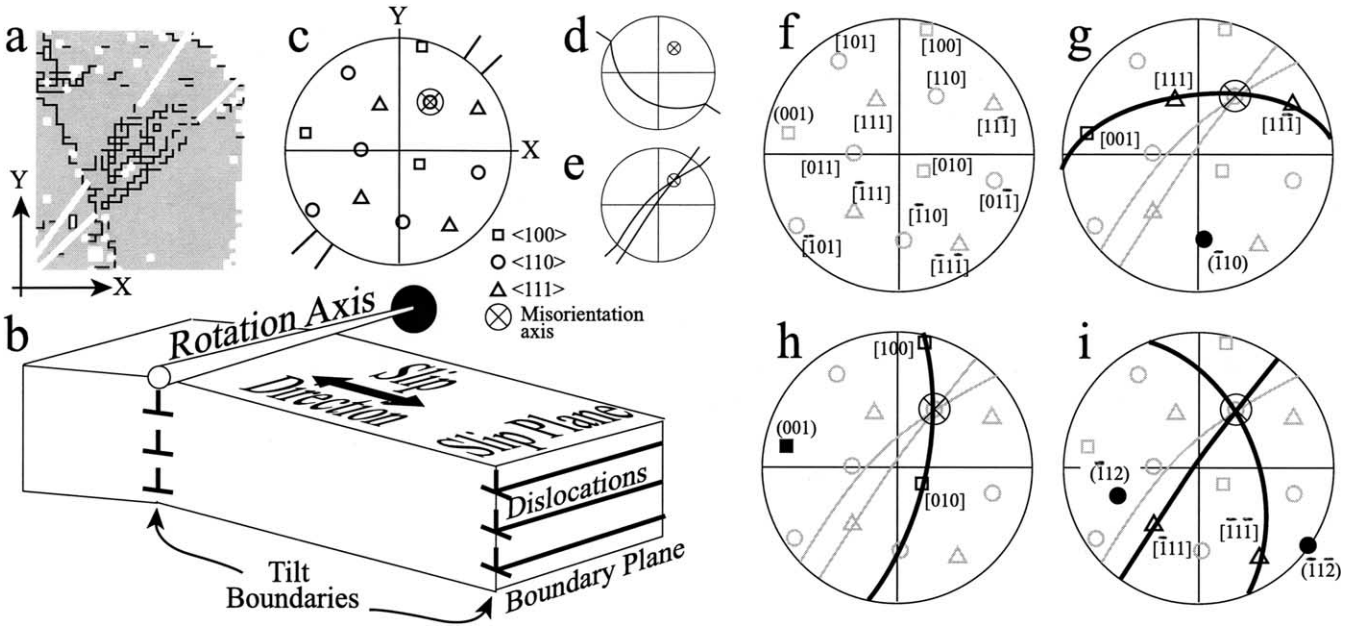

Fig. 9. Dislocation models to explain the low angle boundaries identified in the upper part of the Glenelg garnet (Fig. 2a) and the data dispersions (Fig. 6a) associated with these. (a) Part of the orientation map shown in Fig. 2a showing a set of low angle boundaries (mostly $>2°$ and $<5°$, some $>5°$ and $<10°$). The boundaries are oriented approximately NE–SW: the white lines highlight the trace orientations that can be seen. Arrows show X–Y orientations for comparison with stereonets. (b) 3D cartoon of two parallel tilt walls to show the relative orientations of boundary plane, slip plane, slip direction and misorientation axes. (c) Lower hemisphere equal area stereonet to show the orientation of the grain that contains the boundaries of interest. The dispersion of the data is not shown although the interpreted misorientation axis (Fig. 6a) is marked. Lines extending outward from the primitive circle show the boundary trace orientations highlighted in (a). X and Y directions are shown and are the same for all the other stereonets in this figure. (d) The great circle shows the approximate boundary plane orientation (orthogonal to the misorientation axis) predicted if the boundaries are twist walls. Lines extending outward from the primitive circle show the boundary trace orientations expected if the boundaries are twist walls. (e) Great circles show the boundary plane orientations, reconstructed from the misorientation axis and the observed trace orientations (lines extending outward from the primitive circle), assuming that the boundaries are tilt walls. (f) Stereonet as plotted in (b), but with all $\langle 100\rangle$, $\langle 110\rangle$ and $\langle 111\rangle$ labelled to help the reader understand (g)–(i). (g)–(i) show the geometries of known garnet dislocations (Voegelé et al., 1998a,b) in the context of the grain of interest. Greyed great circles show the reconstructed boundaries assuming a tilt wall model (see (b)). The small squares, circles and triangles are crystallographic orientations (see key to (c)). Black symbols show the slip vector (hollow symbol: labelled with square brackets) and poles to slip plane (solid symbol: labelled with curved brackets). The slip plane is shown as a black great circle. The misorientation axis is marked by the larger circle and cross. (g) $\langle 100\rangle\{011\}$ and $\frac{1}{2}\langle 111\rangle\{1-10\}$ dislocation geometry. The (-110) plane (that contains the misorientation axis), contains [001] and two slip vectors [111] and $[11-1]$. (h) $\langle 001\rangle\{001\}$ dislocation geometry. For the (001) plane (that contains the misorientation axis), there are two slip vectors [010] and [100]. (i) Geometry of $\frac{1}{2}\langle 111\rangle\{11-2\}$ dislocations. There are two $\{11-2\}$ planes that contain the misorientation axis. Each of these contains one $\langle 111\rangle$ direction.

one reconstructed subgrain boundary plane and has an angle of 10° to the other (Fig. 9i). The boundary is unlikely to comprise $\frac{1}{2}[-111](-11-2)$ edge dislocations. The (-112) plane has angles of 70 and 80° to the reconstructed subgrain boundary planes (Fig. 9i) and the boundaries may comprise $\frac{1}{2}[-11-1](-112)$ edge dislocations.

If the assumptions implicit in the analysis presented above are reasonable, the boundaries are best explained as tilt walls of one of the symmetric variants of the $\frac{1}{2}\langle 111\rangle\{1-12\}$ slip system (the $\frac{1}{2}[-11-1](-112)$ slips system using the convention set up in Fig. 9c). This geometrical analysis needs verifying by 3D reconstruction of boundary planes and by TEM characterisation of dislocation populations. It may prove too simplistic an approach, but if verifiable provides a powerful tool for constraining slip systems across small volumes of deformed grains.

4.2. Alpine garnet

In the Alpine garnet, the constant orientation within orientation domains suggests that there is no plastic deformation of the lattice. If this garnet has been deformed then recovery, dynamic recrystallisation or static annealing have removed the evidence for plastic deformation. The garnet shape does not suggest strain high enough to explain the observed boundary misorientations. Moreover, the random misorientations suggest that the boundaries are not subgrain boundaries formed by the recovery of dislocations. It is feasible that high angle boundaries that have formed by strain-induced grain boundary migration could have random misorientations. However, Trimby et al. (1998) show that high angle ($\gg 15°$) recrystallised quartz grain boundaries often have crystallographically controlled misorientation axes. Typically deformation and associated recovery and recrystallisation give rise to core and mantle structures with coarse grains in the core and finer grains in the rim. Spiess et al. (2001) report that the preferred orientations of different porphyroblasts in the same sample are different. Overall, the data suggest that this garnet has never been plastically deformed.

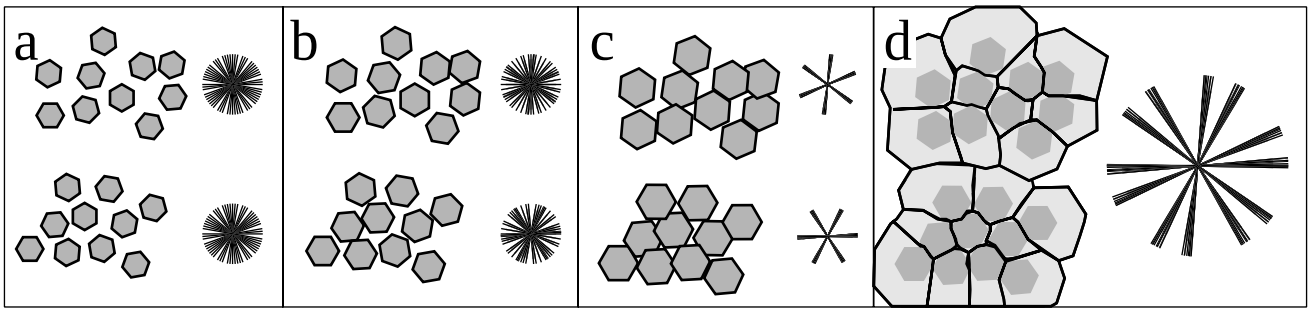

Fig. 10. Cartoon to show the development of a garnet porphyroblast containing two clusters, with subtly different preferred orientations, using the coalesence and boundary energy driven rotation model of Spiess et al. (2001). (a) 2D hexagonal objects are used to represent garnet grains that have nucleated in random orientations in two closely spaced clusters. Rose diagrams show the orientation distributions for each of the clusters (there are three lines for each grain in the rose diagrams). (b) Growth on the existing nuclei causes some of the grains in each cluster to come into contact with each other. As two grains touch, one of the grains (chosen arbitrarily) is rotated to the approximate orientation of the other. The order in which touching grains are considered affects the outcome, as when one grain touches an aggregate of grains (or a small aggregate touches a larger aggregate) the single grain (or smaller aggregate) is rotated to the orientation of the larger aggregate. The kinetic model presented by Spiess et al. (2001) predicts that smaller grains will rotate more rapidly than large grains. The rose diagrams show that each cluster has developed a weak preferred orientation. (c) After further growth, garnet grains in each cluster are all touching. There has been no attempt to draw realistic contacts between garnet grains in this cartoon (contrast with Fig. 22 of Spiess et al., 2001), hexagons overlap each other in an arbitrary manner. The rose diagrams now show strong preferred orientations in each cluster. (d) Sketch of the microstructure after sufficient further growth that the two clusters have coalesced. The kinetics of rotation of the clusters will be slow, as they are large and in this cartoon, the clusters have not been rotated relative to each other. The rose diagram shows the bimodal preferred orientation for the porphyroblast as a whole. Each of the original clusters is represented by a centre of fine garnet grains and a margin of coarser garnet grains.

Peruzzo (1998) and Spiess et al. (2001) present X-ray compositional map data that suggest that the Alpine garnet porphyroblasts formed by coalescence of garnets that grew from many individual nuclei. The constant orientation within orientation domains mapped here are consistent with each orientation domain corresponding to growth on an individual garnet nucleus. The distribution of fine grains in the core and coarse in the margin can be explained by differential growth rates after nucleation (Spiess et al., 2001).

The multiple nucleation and coalescence model, in the absence of other processes, does not explain the strong CPO. The random pair misorientation angle distribution is that expected purely as a function of the CPO. The misorientation angles of neighbouring garnet grains have a stronger bias towards low angles than can be explained by the overall CPO. Spiess et al. (2001) suggest that when one garnet grain touches a neighbour, relative physical rotation of the two grains occurs to reduce the misorientation magnitude at their mutual boundary (op cit). The process is driven by boundary energy, which is lower for smaller misorientations (Sutton and Baluffi, 1987), and is facilitated by diffusion (op cit.). The details of the neighbour pair misorientation angle distributions should be predictable by numerical models and will provide a valuable test of the model (Wheeler et al., 2001).

This porphyroblast has two clusters of orientations, corresponding to the upper blue–grey coloured part of the porphyroblast and the lower yellow coloured part (Fig. 2d). These two areas correspond to the two dominant orientations in the pole figure (Fig. 2f). Statistically, these two clusters are misoriented relative to each other, giving rise to the high angle (~55° peak) in the random pair misorientation distribution. One prediction of the Spiess et al. (2001) model is that coalescence in different parts of the developing porphyroblast should lead to clusters of orientation and Fig. 10 shows a cartoon to illustrate how this might have generated the microstructure observed in this garnet.

5. The significance of garnet microstructures

Garnet is critical to many thermobarometers and major element, trace element and isotopic zoning patterns together with inclusion assemblages are used to infer metamorphic histories (see, for example, Spear, 1994). Many mantle models suggest that majoritic garnet is a major component of the mantle transition zone and may control mantle rheology (Karato et al., 1995). Thus understanding processes within garnet is of particular importance and requires microstructural data.

Initial suggestions that garnet could be deformed came from Laue diffraction studies, of flattened garnets in mylonites, which showed lattice bending consistent with the kinematic framework of the mylonites (Dalziel and Bailey, 1968; Ross, 1973) and etching to reveal dislocation substructures (Carstens, 1969, 1971). The presence of dislocations and subgrains was confirmed by TEM studies (Smith, 1982; Allen et al., 1987; Ando et al., 1993; Doukhan et al., 1994) and we now have a fairly good idea of important slip systems in natural garnets (Voegelé et al., 1998a,b). SEM based studies such as those on mantle garnets (Prior et al., 2000) and the data on the Glenelg garnet presented here show that garnet deformation microstructures can be very significant.

Although garnet creep deformation is significant, OC imaging and SEM based diffraction have also allowed the

documentation of garnet substructures related to fracture (Prior, 1993; Austrheim et al., 1996), multiple nucleation (Spiess et al., 2001; the Alpine garnet here), and growth processes (Daniel et al., 2001; Boyle, Prior and Brenker, unpublished data). Although it is reasonable that plastic deformation of garnet does occur we must be careful not to interpret all garnet microstructures in this way. For example, one area that needs further study is that of shaped garnets in granulite facies rocks. Ji and Martignole (1994) suggested that shaped garnets in granulites relate to plastic deformation and this alone seems reasonable since we can now document lower-grade plastically deformed garnets. This paper has provoked much discussion (Den Brok and Kruhl, 1996; Ji and Martignole, 1996) as the model requires garnet to be weaker than both quartz and feldspar. Although Ji and Martignole (1994) showed that these garnets contain subgrains, subsequent analysis using OC imaging (Prior and Ji, unpublished data) and a study of similar garnets from Sri Lanka (Kleinschrodt and McGrew, 2000) show that substructures in these garnets are rare. Kleinschrodt and McGrew (2000) show that these samples have a CPO. The CPOs are, however, very weak and the microstructural data may yet be explained by mechanisms other than plastic deformation that affect both microstructure and CPO development.

6. Orientation mapping using EBSD

The example of the garnet microstructures shows two of the key elements of EBSD analysis:

1. The misorientation information that can be generated by measuring the spatial variation in orientation can be used to test conceptual, numerical or analytical models for the processes that produce a microstructure.
2. Microstructural analysis can be carried out in nearly all crystalline materials.

These aspects are likely to make EBSD a key microstructural tool in the future. Analysis of misorientation data (Wheeler et al., 2001) without manual definition of orientation domains is difficult in minerals where there is a systematic mis-indexing problem. Work is needed to assess systematic mis-indexing problems and to find ways of eliminating these during data processing or, better still, during data acquisition so that misorientation data can be extracted reliably from automatic EBSD data-sets.

Much of the EBSD work in the next decade is likely to focus on boundaries and interfaces. The importance of boundaries and interfaces in controlling processes and physical properties in rocks has long been recognised (Spry, 1969). Many physical properties of rocks are crucially dependent upon the structure and energy of boundaries and interfaces and their triple junction line intersections. The mobility and diffusivity of boundary/interfaces and triple junctions control microstructural development, which in turn, influence the mechanical behaviour during creep and fracture and the ability of fluid phases (including water, hydrocarbons and melt) to permeate the boundaries/interface network. A full understanding of processes such as rock deformation, mineral reactions during metamorphism and fluid transport requires us to understand the role of boundaries, interfaces and triple junctions. A starting point has to be the documentation of boundary and interface geometries. Vernon (1968) completed one of the first thorough analyses of grain boundary geometry in metamorphic rocks. At that time the geometrical analysis was limited by available technology. The development of EBSD creates a new opportunity to understand boundaries and interfaces, as this is the first technique that lets us document boundary and interface misorientations (we can define an analogue of misorientation geometry across an interface) in a statistically significant manner (Faul and Fitz Gerald, 1999; Fliervoet et al., 1999; Wheeler et al., 2001). Although we need boundary/interface plane and curvature data to describe fully the geometry, and to link the geometry to structure and energy, misorientation data alone provide substantial information to help discriminate the role of various processes in forming a microstructure. Wheeler et al. (2001) suggest that neighbour pair misorientation distributions that are different from random pair misorientation distributions mean that a boundary must have characteristics inherited from a pre-existing microstructure or there must have been interaction between grains. Many grain-scale processes will generate predictable neighbour and random-pair misorientation distributions. The current challenge and opportunity is to identify the misorientation geometries that characterise specific material processes.

Acknowledgements

This work was funded by NERC grant no GR3 11768. The CamScan X500 crystal probe was funded by HEFCE through JREI grant JR98LIPR. RS. thanks the CNR–short-term-mobility program 1999 and LP the Accademia dei Lincei for financial support to visit Liverpool. CS is in receipt of a NERC studentship. The manuscript was much improved by the reviews of Greg Hirth and Geoff Lloyd and the editorial guidance of Mike Williams. The printing of colour plates was paid for by the Tectonic Studies group.

References

Adams, B.L., Wright, S.I., Kunze, K., 1993. Orientation imaging: the emergence of a new microscopy. Mettalurgical Transactions A24, 819–831.

Allen, F.M., Smith, B.K., Buseck, P.R., 1987. Direct observations of dissociated dislocations in garnet. Science 238, 1695–1697.

Ando, J., Fujino, K., Takeshita, T., 1993. Dislocation microstructures in naturally deformed silicate garnets. Physics of the Earth and Planetary Interiors 80, 105–116.

Austrheim, H., Erambert, M., Boundy, T.M., 1996. Garnets recording deep crustal earthquakes. Earth and Planetary Science Letters 139, 223–238.

Bartozzi, M., Boyle, A.P., Prior, D.J., 2000. Automated grain boundary

detection and classification in orientation contrast images. Journal of Structural Geology 22, 1569–1579.

Boyle, A.P., Prior, D.J., Banham, M.H., Timms, N.E., 1998. Plastic deformation of metamorphic pyrite: new evidence from electron backscatter diffraction and forescatter orientation contrast imaging. Mineralium Deposita 34, 71–81.

Carstens, H., 1969. Dislocation structures in pyropes from Norwegion and Czech garnet peridotites. Contributions to Mineralogy and Petrology 24, 348–353.

Carstens, H., 1971. Plastic stress relaxation around solid inclusions in pyrope. Contributions to Mineralogy and Petrology 32, 289–294.

Dalziel, I.W.D., Bailey, S.W., 1968. Deformed garnets in a mylonitic rock from the Grenville front and their tectonic significance. American Journal of Science 266, 542–562.

Daniel, C.G., Hirsch, D.M., Prior, D.J., Spear, F.S., Carlson, W.D., 2001. New constraints on growth models for complexly zoned garnet from Harpswell Neck, Maine: crystallographic data from orientation contrast imaging and electron backscatter diffraction. Submitted to American Mineralogist, in review.

Den Brok, B., Kruhl, J.H., 1996. Ductility of garnet as an indicator of extremely high temperature deformation: discussion. Journal of Structural Geology 18, 1369–1373.

Dingley, D.J., 1984. Diffraction from sub-micron areas using electron backscattering in a scanning electron microscope. Scanning Electron Microscopy 2, 569–575.

Dingley, D.J., 2000. The development of automated diffraction in scanning and transmission electron microscopy. In: Schwartz, A., Kuma, M., Adams, B.L. (Eds.). Electron Backscatter Diffraction in Materials. Kluwer Academic Publishing, New York, pp. 1–18.

Doukhan, N., Sautter, V., Doukhan, J.C., 1994. Ultradeep, ultramafic mantle xenoliths — Transmission Electron Microscopy preliminary results. Physics of the Earth and Planetary Interiors 82, 195–207.

Faul, U.H., Fitz Gerald, J.D., 1999. Grain misorientations in partially molten olivine aggregates: an electron backscatter diffraction study. Physics and Chemistry of Minerals 26, 187–197.

Fliervoet, T.F., Drury, M.R., Chopra, P.N., 1999. Crystallographic preferred orientations and misorientations in some olivine rocks deformed by diffusion or dislocation creep. Tectonophysics 303, 1–27.

Fynn, G.W., Powell, W.J.A., 1979. The Cutting and Polishing of Electro–Optic Materials. Adams Hilger, London, 216pp.

Humphreys, F.J., Bate, P.S., Hurley, P.J., 2001. Orientation averaging of EBSD data. Journal of Microscopy 201, 50–58.

Ji, S., Martignole, J., 1994. Ductility of garnet as an indicator of extremely high temperature deformation. Journal of Structural Geology 16, 985–996.

Ji, S., Martignole, J., 1996. Ductility of garnet as an indicator of extremely high temperature deformation: reply. Journal of Structural Geology 18, 1375–1379.

Karato, S., Wang, Z., Liu, B., Fujino, K., 1995. Plastic deformation of garnets: systematics and implications for the rheology of the mantle transition zone. Earth and Planetary Science Letters 130, 13–30.

Kleinschrodt, R., McGrew, A., 2000. Garnet plasticity in the lower continental crust: implications for deformation mechanisms based on microsctructures and SEM-electron channelling pattern analysis. Journal of Structural Geology 22, 795–809.

Leiss, B., Barber, D., 1999. Mechanisms of dynamic recrystallization in naturally deformed dolomite inferred from EBSP analyses. Tectonophysics 303, 51–69.

Leiss, B., Ullemeyer, K., Weber, K., Bunge, H.-J., Casey, M., Drury, M., Frischbutter, A., Fueten, F., Klein, H., Kuhs, W., Lloyd, G.E., Mainprice, D., Montoto, M., Prior, D.J., Wenk, H.-R., 2000. Actual and future developments and goals in texture research of geological materials. Journal of Structural Geology 22, 1531–1540.

Lloyd, G.E., 1987. Atomic number and crystallographic contrast images with the SEM: a review of backscattered techniques. Mineralogical Magazine 51, 3–19.

Lloyd, G.E., Freeman, B., 1991. SEM electron channelling analysis of dynamic recrystallization in a quartz grain. Journal of Structural Geology 13, 945–953.

Lloyd, G.E., Freeman, B., 1994. Dynamic recrystallization of quartz and quartzites. Journal of Structural Geology 16, 867–881.

Lloyd, G.E., Farmer, A.B., Mainprice, D., 1997. Misorientation analysis and the formation and orientation of subgrain and grain boundaries. Tectonophysics 279, 55–78.

Peruzzo, L., 1998. Studio di caratteri distintivi fra il Complesso di Monteneve e il Complesso di Merano-Mules nell'area tra Cima Fiammante, L'Altissima e il Similaun. PhD thesis (unpublished), Dipartimento di Mineralogia e Petrologia, Università di Padova.

Prior, D.J., 1993. Sub-critical fracture and associated retrogression of garnet during mylonitic deformation. Contributions to Mineralogy and Petrology 113, 545–556.

Prior, D.J., 1999. Problems in determining misorientation axes, for small angular misorientations, using electron backscatter diffraction in the SEM. Journal of Microscopy 195, 217–225.

Prior, D.J., Trimby, P.W., Weber, U.D., Dingley, D.J., 1996. Orientation contrast imaging of microstructures in rocks using forescatter detectors in the scanning electron microscope. Mineralogical Magazine 60, 859–869.

Prior, D.J., Boyle, A.P., Brenker, F., Cheadle, M.C., Day, A., Lopez, G., Peruzzo, L., Potts, G.J., Reddy, S.M., Spiess, R., Trimby, P.W., Wheeler, J., Zetterström, L., 1999. The application of Electron Backscatter Diffraction and Orientation Contrast Imaging in the SEM to textural problems in rocks. American Mineralogist 84, 1741–1759.

Prior, D.J., Wheeler, J., Brenker, F.E., Harte, B., Matthews, M., 2000. Crystal plasticity of natural garnet: new microstructural evidence. Geology 28, 1003–1006.

Randle, V., Engler, O., 2000. Introduction to Texture Analysis: Macrotexture, Microtexture and Orientation Mapping. Gordon & Breach Science Publishers, Reading, UK.

Ross, J.V., 1973. Mylonitic rocks and flattened garnets in the southern Okanagan of British Columbia. Canadian Journal of Earth Sciences, 10, 1–17.

Schwartz, A., Kuma, M., Adams, B.L., 2000. Electron Backscatter Diffraction in Materials. Kluwer Academic Publishing, New York.

Smith, B.K., 1982. Plastic deformation of gernets: mechanical behaviour and associated microstructures. Unpublished PhD. University of California, Berkeley.

Spear, F.S., 1994. Metamorphic phase equilibria and pressure–temperature–time paths. Mineralogical Society of America, Monograph, 799 pp.

Spiess, R., Peruzzo, L., Prior, D.J., Wheeler, J., 2001. Development of garnet porphyroblasts by multiple nucleation, coalescence and boundary misorientation driven rotations. Journal of Metamorphic Geology 19, 269–290.

Spry, A., 1969. Metamorphic Textures. Pergamon Press, Oxford.

Sutton, A.P., Baluffi, R.W., 1987. On geometric criteria for low interfacial energy. Acta Metallurgica 35, 2177–2201.

Trimby, P.W., Prior, D.J., Wheeler, J., 1998. Grain boundary hierarchy development in a quartz mylonite. Journal of Structural Geology 20, 917–935.

Venables, J.A., Harland, C.J., 1973. Electron backscattering patterns — a new technique for obtaining crystallographic information in the SEM. Philosophical Magazine 27, 1193–1200.

Vernon, R.H., 1968. Microstructures of high-grade metamorphic rocks at Broken Hill, Australia. Journal of Petrology 9, 1–22.

Voegelé, V., Ando, J.I., Cordier, P., Liebermann, R.C., 1998a. Plastic deformation of silicate garnet I. High pressure experiments. Physics of the Earth and Planetary Interiors 108, 305–318.

Voegelé, V., Cordier, P., Sautter, V., Sharp, T.G., Lardeaux, J.M., Marques, F.O., 1998b. Plastic deformation of silicate garnets II. Deformation microstructures in natural samples. Physics of the Earth and Planetary Interiors 108, 319–338.

Wheeler, J., Prior, D.J., Jiang, Z., Spiess, R., Trimby, P.W., 2001. The petrological significance of misorientations between grains. Contributions to Mineralogy and Petrology 141, 109–124.